Computational Study of Aerodynamics and Noise of Quadrotor AAV in Full Configuration with Different Rotor Arm Angles

Yu-Hyeon Hwang, Si Jin Kim, Hyeon-Su Song, Rho Shin Myong, Hakjin Lee
Gyeongsang National University, Jinju, Republic of Korea

Abstract

This paper investigates the aerodynamic and acoustic characteristics of an advanced air vehicle (AAV) in full configuration in hover. Quadrotor configuration with different positions of the rear rotors is considered to study the rotor interactional effect on the aerodynamic performance, wake structure, and noise levels. The positions of rear rotors are controlled by changing the rotor arm angles of the rear rotor from 0° to 20°. The lattice-Boltzmann method (LBM) is utilized for the aerodynamic analysis, and the acoustic analogy based on Ffowcs Williams-Hawkings (FW-H) equation is used for evaluating noise level. The computational analysis revealed that the interactional phenomena intensified as the rotor arm angles of rear rotor increases, leading to significant thrust fluctuation and higher noise levels. The findings in this study help to improve our understanding of interactions between rotors and optimize the configuration that maximizes the aerodynamic efficiency and minimizes noise levels, contributing to the advancement of AAV technology and its acceptance in urban environments.

1. NOTATION

Symbols

R	Rotor radius, ft
ϕ	Fuselage tilt angle, deg
V_∞	Freestream velocity, kt
Δf	Frequency resolution, Hz
θ	Rear rotor angle, deg
C_{tip}	Tip chord length, ft
ψ	Rotor azimuth angle, deg

Acronyms:

CFD	Computational Fluid Dynamics
CAA	Computational Aeroacoustics
CW	Clockwise Rotation
CCW	Counterclockwise Rotation
SPL	Sound Pressure Level, dB
OASPL	Overall Sound Pressure Level, dB
DEP	Distributed Electric Propulsion
AAV	Advanced Air Vehicle
eVTOL	Electric Vertical Take-off and Landing

2. INTRODUCTION

Recently, the development of advanced air vehicle (AAV) with capability of electric vertical take-off and landing (eVTOL) has gained significant attention to resolve the growing traffic congestion in metropolitan areas. eVTOL has been proposed more than 1,000 different models, including prototypes and demonstrator (Ref. 1~3). AAV primarily is equipped with distributed electric propulsion (DEP) system, which can achieve propulsor redundancy, improve the aerodynamic efficiency, and reduce carbon emission and environmental noise (Ref. 4). However, the multiple distributed rotor systems lead to the aerodynamic interference between rotor-rotor and rotor-airframe. Zhou et al. conducted the aerodynamic measurement on a small unmanned aerial vehicle (UAV) in wind tunnel facility by varying the speation distance between the adjacent rotors. They also discovered that thrust fluctuation increased as the rotor spacing increases. Piccinini et al. (Ref. 6) executed computational analyses of multiple rotors with different rotor arrangements. In tandem configuration, thrust loss increased by up to 40% due to rotor interactions. Herz et al. (Ref. 7) performed wind tunnel tests on a small quadrotor in forward flight to compare thrust coefficients based on substitution with the skew angles of quadrotor and the rotor rotation directions. Alvarez and Ning (Ref. 8) presented multirotor vortex particle model and identified rotor-on-rotor interaction. They captured the thrust drop and unsteady loading produced by rotor interaction. Stokkermans et al. (Ref. 9) demonstrated that the interaction between rotors can reduce thrust by up to 30% in forward flight. As in previous studies, rotor interaction is a critical factor in determining the aerodynamic performance of AAV, and the arrangement of rotor is one of the important design parameters.

In designing an AAV, various requirements need to be considered for public acceptance. Noise radiated from AAV is one of the main barrier to widespread use of AAV, and various methods were introduced to predict noise sources of aircraft (Ref. 10~12). Casalino et al. (Ref. 13, 14) analyzed noise sources for eVTOL, identifying the changes in community noise and scattering effect with various flight paths. Yunus et al. (Ref. 15) used a noise sphere to predict the noise of UAM in an urban vertiport environment. They accounted for a low-fidelity approach that can efficiently calculate the noise footprint, considering various design variables and operational conditions. Jia and Lee (Ref. 16) conducted noise analysis on a full-configuration quadrotor and found that the self-BVI event leads to changes in sound pressure level (SPL). Lee and Lee (Ref. 17) conducted a computational noise analysis based on different multirotor configuration. As the the rotors are located in close proximity to each other, there is an increase in thrust fluctuation and SPL due to unsteady loading. Jia and Lee (Ref. 18) examined impact of overlap distance of side-by-side eVTOL with high-fidelity CFD simulations. They found that as the overlap size increases, the rotor-to-rotor BVI interaction becomes stronger, increasing to the negative peak of acoustic pressure. Zhang et al. (Ref. 19) conducted the noise analysis of the eVTOL configurations with the different number of propeller, and it was found that the wake of the front propellers influences the rear wing and propellers, leading to an increase in noise level and radiation. Afari and Mankbadi (Ref. 20) compared the noise of multi-rotors in hovering and forward flight conditions. They identified that interaction between the tip vortex of the front rotor and the rear rotor induces an increase in broadband noise.

In this study, the computational analysis was performed to evaluate the aerodynamic and noise of quadrotor AAV in full configuration with different rear rotor locations in hovering. The effects of the rear rotor location on the thrust fluctuation, wake evolution, flow field and noise levels were investigated by changing the rear rotor arm angles, while the location of the front rotor was fixed. The computational analysis was conducted using the PowerFLOW, which is a high-fidelity numerical analysis based on the lattice-Boltzmann method (LBM).

3. Numerical methodology

3.1. Lattice-Boltzmann methods (LBM)

LBM is the method that discretizes the Boltzmann equation, which is well-known in statistical mechanics, and presents the discretized particles as variables in the form of distribution functions. It numerically calculates the collision and movement processes of particles. Compared to the Navier-Stokes equations, which calculate nonlinear partial differential equations, LBM models the dynamic movement of microscopic particles and derives values for macroscopic physical quantities through algebraic equations. Through this method, fluid physical quantities can be calculated simply and efficiently. It is also well-suited for parallel processing and three-dimensional expansion, making it useful for analyzing the characteristics of serration and porous material (Ref. 21, 22). The lattice model used in LBM is DaQb, where "a" indicates the range of dimensions, and "b" denotes the number of possible paths for particle movement. This study selected the D3Q19 model to present 19 directions in three dimensions, and Figure 1 presents the discretized lattice and particle movements (Ref. 23).

Considering the discretized space, the lattice-Boltzmann equation can be defined in Eq. (1). f_i is the distribution function of particles at position x with their movement, and c_i denotes the velocity vector of particles in the i-direction. Ω_i is the collision term due to particle interactions, and it is defined as shown in Eq. (2) using the Bhatnagar-Gross-Krook (BGK) model (Ref. 24, 25).

(1) $$f_i(\vec{x}+\vec{c}_i\Delta t, t+\Delta t) - f_i(\vec{x},t) = \Omega_i(f(\vec{x},t))$$

(2) $$\Omega_i(f(\vec{x},t)) = -\frac{1}{\tau}[f_i(\vec{x},t) - f_i^{eq}(\vec{x},t)]$$

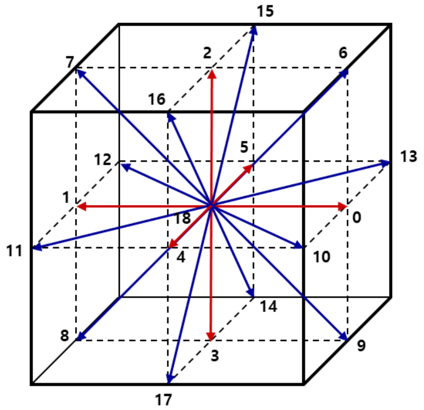

Figure 1: D3Q19 model for LBM simulation

In Eq. (2), τ means the relaxation time, the dimensionless time required for particles to reach an equilibrium state after a collision. Its relationship with the kinematic viscosity (υ) is defined in Eq. (3). τ must be greater than 0.5, and C_s means the lattice speed of sound.

(3) $$\upsilon = (\tau - \frac{1}{2})C_s^2$$

f_i^{eq} is the local equilibrium distribution function that connects the velocity distribution of microscopic particles to macroscopic condition. f_i^{eq} can be expressed by Eq. (4) based on the D3Q19 model by expanding the Maxwell-Boltzmann distribution function, which distributes the particle velocity depending on probability up to the second-order term of velocity in the Taylor series (Ref. 26). u is the macroscopic velocity, and ω_i is the weight factor in the i-direction, which is defined in Eq. (5) depending on the particle direction.

(4) $$f_i^{eq}(\vec{x},t) = \rho\omega_i[1 + 3(\vec{c}_i \cdot \vec{u}) + \frac{9}{2}(\vec{c}_i \cdot \vec{u})^2 - \frac{3}{2}|\vec{u}|^2]$$

(5) $$\omega_i = \begin{cases} 2/36 \ (i = 0,...,5) \\ 1/36 \ (i = 6,...,17) \\ 12/36 \ (i = 18) \end{cases}$$

In Eq. (1), the macroscopic physical quantities at each lattice position, such as density, momentum, energy, and pressure, are defined as follows.

(6) $$\rho(\vec{x},t) = \sum_i f_i(\vec{x},t)$$

(7) $$\rho\vec{u}(\vec{x},t) = \sum_i \vec{c}_i f_i(\vec{x},t)$$

(8) $$E(\vec{x},t) = \sum_i \frac{1}{2}m[\vec{c}_i \cdot \vec{c}_i] f_i(\vec{x},t)$$

(9) $$p = \rho C_s^2$$

LBM requires extending the relaxation time of the BGK model's collision operator for the turbulence modeling. The extended relaxation time can be derived through the Renormalization Group (RNG) theory, finally it can be defined as a function of the turbulent kinetic energy (k) and the turbulent dissipation rate (ε). This approach is referred to as LBM-very large eddy simulation (LBM-VLES) (Ref. 24, 27). RNG $k-\varepsilon$ model is used to calculate the turbulent viscosity relaxation time, and the effective viscosity relaxation time is defined in Eq. (10) (Ref. 28). Here, $C_\mu = 0.09$, μ is based on a local strain parameter, a local vorticity parameter, and local helicity parameters (Ref. 29).

(10) $$\tau_{eff} = \tau + C_\mu \frac{k^2/\varepsilon}{\sqrt{(1+\tilde{\mu}^2)}}$$

Our research team used LBM to predict the aerodynamic performance of rotor blades and compared the sound level and radiation of tonal noise resulting from rotor-airframe interactions (Ref. 30). This study utilized the LBM-VLES to simulate the complex turbulent flow developed through the interactions of vortices generated by each rotor.

3.2. Acoustic analogy

This study employed the acoustic analogy based on the Ffowcs Williams-Hawkings (FW-H) equation to predict the noise radiated from a quadrotor AAV aircraft. FW-H equation can consider the rotating objects within the flow field, based on Lighthill's acoustic analogy (Ref. 31). FW-H equation is defined in Eq. (11). The first term on the right-hand side presents turbulence noise, the second presents loading noise, and the third term presents thickness noise. Turbulence noise is effective when the blade tip Mach number is transonic or supersonic. This study investigates acoustic analysis in subsonic, so turbulence noise is neglected, and only thickness noise and loading noise are considered (Ref. 32). The sound pressure level of thickness noise and loading noise was evaluated using Farassat formulation 1A, as defined in Eq. (12) and Eq. (13), respectively (Ref. 33).

(11)
$$4\pi p'(x,t) = \frac{\partial^2}{\partial x_i \partial x_j}\iiint\left[\frac{T_{ij}}{r|1-M_r|}\right]dV - \frac{\partial}{\partial x_i}\iint\left[\frac{p_{ij}n_j}{r|1-M_r|}\right]dS + \frac{\partial}{\partial t}\iint\left[\frac{\rho_\infty v_n}{r|1-M_r|}\right]dS$$

(12)
$$4\pi p'_T(\vec{x},t) = \int_{f=0}\left[\frac{\rho_0(\dot{v}_n + v_{\dot{n}})}{r|1-M_r|^2}\right]_{ret} dS + \int_{f=0}\left[\frac{\rho_0 v_n(r\dot{M}_r + a_0 M_r - a_0 M^2)}{r^2|1-M_r|^3}\right]_{ret} dS$$

(13)
$$4\pi p'_L(\vec{x},t) = \frac{1}{a_0}\int_{f=0}\left[\frac{\dot{l}_r}{r|1-M_r|^2}\right]_{ret} dS + \int_{f=0}\left[\frac{l_r - l_M}{r^2|1-M_r|^2}\right]_{ret} dS + \frac{1}{a_0}\int_{f=0}\left[\frac{l_r(r\dot{M}_r + a_0 M_r - a_0 M^2)}{r^2|1-M_r|^3}\right]_{ret} dS$$

4. Numerical simulation setup

4.1. Quadrotor model

In this study, a six-passenger quadrotor AAV designed by NASA was considered, and its geometric information was provided from OpenVSP (Ref. 34). The quadrotor AAM geometry and the computational domain are depicted in Figure 2. The rotor blade has four blades with the radius (R) of 15 feet. The right front (RF) and left rear (LR) rotors rotate counterclockwise (CCW), while the left front (LF) and right rear (RR) rotors rotate clockwise (CW) to maintain the yawing moment as depicted in Figure 3.

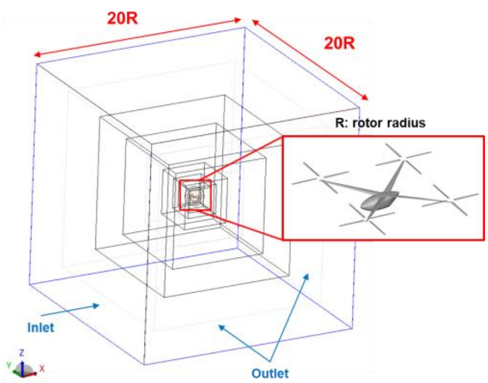

Figure 2: Computational domain with quadrotor model

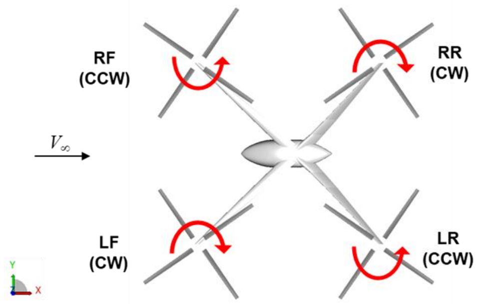

Figure 3: Rotor setup of quadrotor

4.2. Computational analysis setup

The computational domain for LBM simulation is set to 20 rotor radii (300 ft) based on the rotor radius and specific grid system is depicted in Figure 4. The surface gird is set with high density along the leading and trailing edges of the blades, as displayed in Figure 4(a). The finest grid cells are constructed in the near-field of blades within the volume grid, as depicted in Figure 4(b). Variable resolution (VR) is used when configuring the grid domain, setting 14 layers. The grid size doubles with each layer, starting from the layer containing the finest grid. The finest grid size used is 0.02 ft, 2.5% of the blade tip chord length. Approximately 900 million grid cells are used. The time step size for the unsteady analysis is set to 0.02° based on rotor. The computational domain was internally calculated by PowerFLOW, using a Courant-Friedrichs-Lewy (CFL) number of 1, which is according to the finest grid size (Ref. 35).

The sliding mesh method is used to apply rotational effects for each rotor. No-slip boundary conditions are imposed on fuselage and rotors to consider the viscous effect. Velocity and pressure inlet condition and pressure outlet condition are defined for boundary conditions. The rotational speed of each rotor is fixed at 350 RPM, with a tip Mach number of 0.4. Aerodynamic data are collected at 5° intervals, and data for noise analysis are collected at 0.04° intervals for computational efficiency. Standard temperature and atmospheric pressure is used. Aerodynamic analysis of quadrotor AAV in hover is conducted for 18 rotor revolutions, and the results for the last 5 revolution are used for acoustic analysis, which correspond to the frequency resolution of 1.2 Hz. The position of the rear rotor is set by adjusting the rear rotor arm angle (θ), as shown in Figure 5. The initial setup is established with identical angles for both the front and rear rotor arms, and the angle of the rear rotor arms is modified in a counterclockwise direction to θ = 0°, 5°, 10°, and 20°.

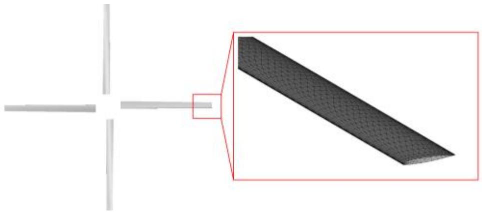

(a) Surface grid

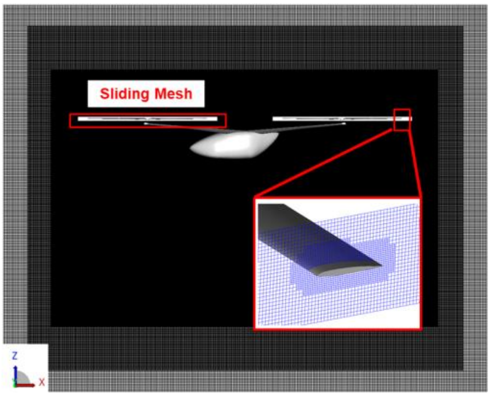

(b) Volume grid

Figure 4: Computational grid system for quadrotor configuration

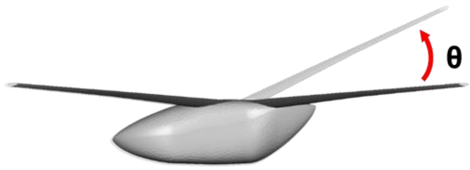

Figure 5: Rear rotor arm angle transition

Microphones are placed ten rotor radii (150 ft) below the quadrotor configuration for noise analysis to measure the noise level that affects far-field receivers. Figure 6(a) shows that 12 microphones are arranged at the spacing of 30° in azimuth. Additionally, to confirm the noise directivity in the bottom region of the configuration, a total of 325 microphones are placed five rotor radii (75 ft) below the configuration at the spacing of 10°, as depicted in Figure 6(b).

5. Numerical results

5.1. Grid resolution test

A grid resolution test is performed to ensure efficient numerical analysis before employing the aerodynamic and aeroacoustic investigation. Based on the case with the rotor arm angle of θ = 0°, the total number of grid cells is varied, and the thrust of the last revolution is compared. The total number of grid cells is changed depending on the size of the finest grid, and grid resolution test is performed for five cases, as shown in Table 1 and Figure 7.

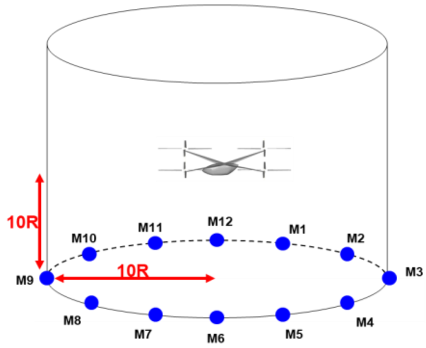

(a) Azimuth angle

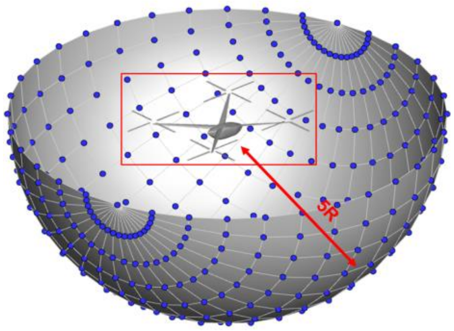

(b) Noise hemisphere

Figure 6: Microphone array with azimuth angle and noise hemisphere

All computational simulations are performed on 191 CPU cores in parallel on the high-performance computing (HPC) cluster. The ratio of the tip chord length determines the size of the finest grid, and it is observed that the thrust tends to increase as the size of the finest grid becomes smaller. When the number of grid cells increases from 500 million to 900 million, the thrust increases by 10%. However, when the grid cells increase from 900 million to 1.7 billion, the thrust increases by 0.6%. The rate of thrust increase is confirmed to be a substantial decline, indicating a trend toward convergence in thrust when the number of grid cells exceeds 900 million. Consequently, the finest grid size corresponding to 2.5% of the tip chord length is selected for the computational analysis.

Table 1: Information of grid test

Finest grid size	Total cells	Time [h]	Thrust [N]
7% C_{tip}	40 mil.	6.5	22,000
5% C_{tip}	112 mil.	9.3	24,000
3% C_{tip}	493 mil.	46.6	29,000
2.5% C_{tip}	900 mil.	81.9	31,800
2%	1.7 bil.	118	32,000

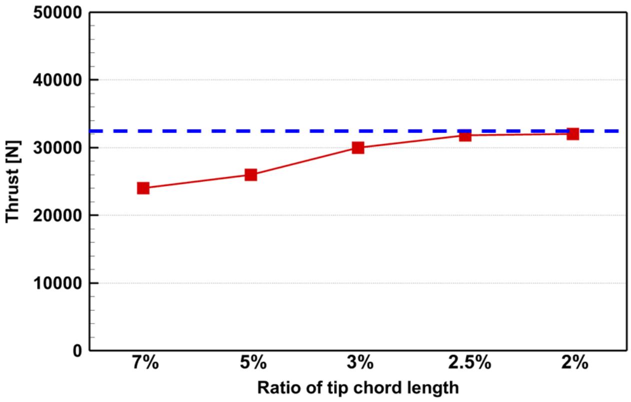

Figure 7: Grid test with rotor thrust

5.2. Numerical results of hovering

This section evaluates the aerodynamic characteristics based on the rear rotor arm angle in hovering. First, vorticity magnitude contours of the right rotors are compared with the position of the rear rotor to demonstrate the interactions between the rotors, as depicted in Figure 8. The left rotor of Figure 8 corresponds to the front rotor, and the right corresponds to the rear. As shown in Figure 8(d), θ = 20° means that the rear rotor is positioned highest. As the height of the rear rotor increases, the vorticity magnitude in the front rotor region becomes stronger and more widespread. This strong vorticity magnitude directly influences the front rotor, as identified in Figure 8(d). This phenomenon explains that as the rear rotor is positioned higher, the wake of the rear rotor is ingested into the wake of the front rotor, resulting in an increased vorticity magnitude.

The thrust fluctuation graph of the front and rear rotors is depicted in Figure 9 to verify the impact of wake interference on the rotors. Figure 9 shows the thrust fluctuation of the LF rotor and the LR rotor. As the height of the rear rotor increases, Figure 9(a) illustrates distinct thrust fluctuation in the front rotor. This is likely because wake interaction influences the front rotor, and this event imposes unsteady and asymmetric loading on the front rotor. On the other hand, Figure 9(b) shows that as the rear rotor is positioned higher, the impact of wake interference on the rear rotor decreases, leading to a slight reduction in thrust fluctuation. As shown in Figure 9, the mutual interaction between rotor wake directly influences the thrust

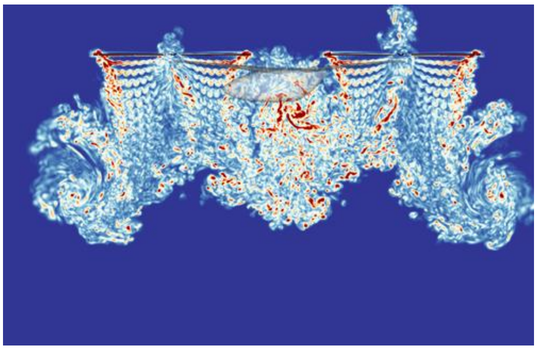

(a) θ = 0°

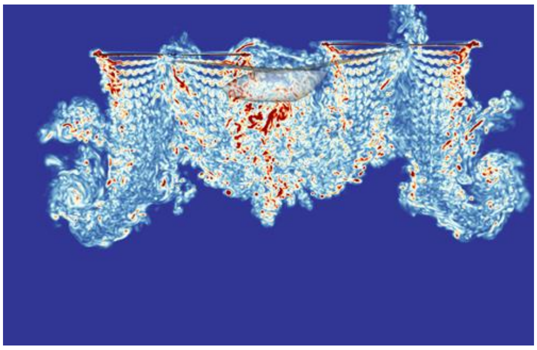

(b) θ = 5°

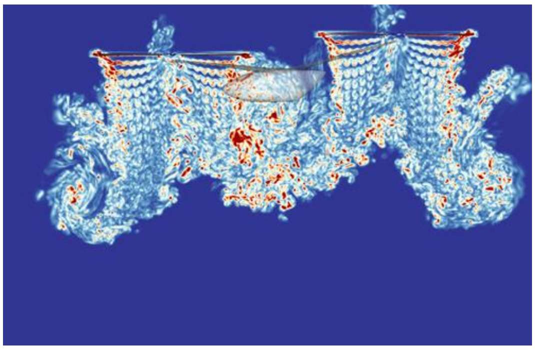

(c) θ = 10°

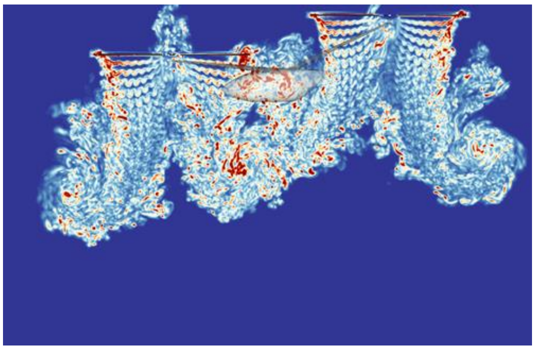

(d) θ = 20°

Figure 8: Comparison of vorticity magnitude with different location of rear rotor

of the front rotor, and the impact of this phenomenon on noise is addressed later.

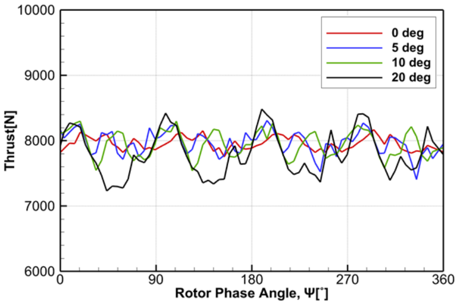

(a) Front rotor

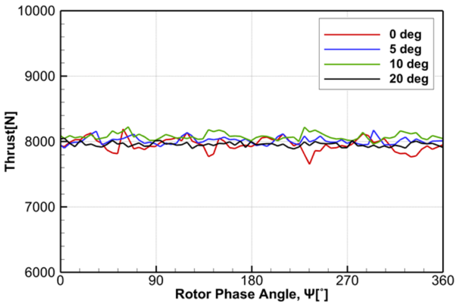

(b) Rear rotor

Figure 9: Thrust fluctuation with different location of rear rotor

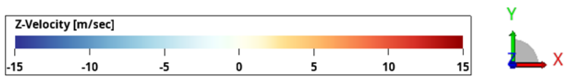

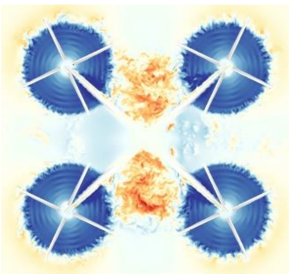

(a) θ = 0°

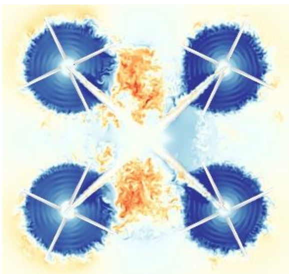

(b) θ = 5°

(c) θ = 10°

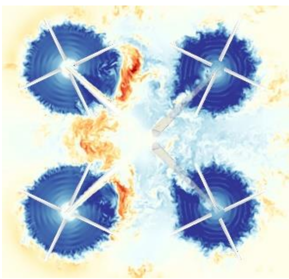

(d) θ = 20°

Figure 10: Comparison of z-velocity with different location of rear rotor

As depicted in Figure 10, the upwash and downwash are evaluated using the z-velocity contour to demonstrate the interference between rotor wake. The comparison is confirmed in the region between the fuselage and the rotor at z = 0.1R (1.5 ft). The left rotor of Figure 10 corresponds to the front rotor, and the right corresponds to the rear. The red flow indicates upwash flow caused by the interaction of the rotor wake, and as the height of the rear rotor increases, the upwash flow approaches the front rotor. As shown in Figure 10(d), the upwash flow is observed to interfere with the blue downwash flow. This interaction affects the aerodynamics of the front rotor and is estimated to cause thrust fluctuation, as shown in Figure 9(a). Also, depending on the rear rotor arm angle, the flow velocity of the rear rotor tends to converge towards the center of rotation.

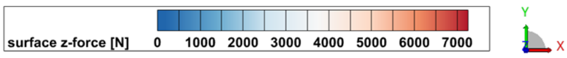

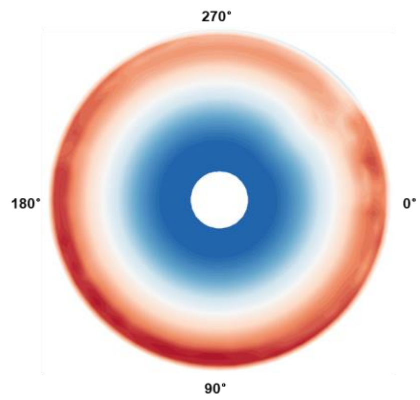

(a) θ = 0°

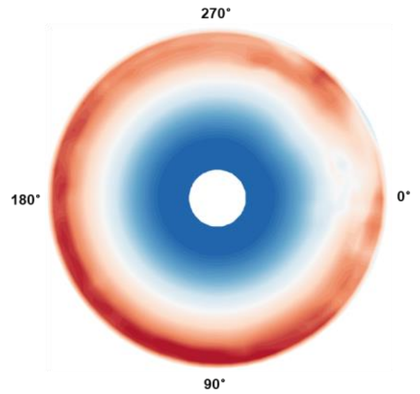

(b) θ = 20°

Figure 11: Thrust disk of left front rotor with different location of rear rotor

The thrust disk of the front rotor is shown in Figure 11 to examine the impact of wake interference on the front rotor. The thrust disk is compared when the rear rotor arm angle is θ = 0° and θ = 20°, showing the LF rotor during the last revolution. In the region between ψ = 270° and 0°, slightly lower thrust is observed, and it is compared to the region between ψ = 90° and 180°. The region between ψ = 270° and 0° is where wake interaction occurs, and this is likely because wake interaction results in an unsteady flow that decreases the effective angle of attack on the front rotor, leading to lower thrust. Figure 12 presents the thrust at the blade tip according to the azimuth angle. The thrust disparity of θ = 0° and θ = 20° is observed from ψ = 300° to ψ = 40°. When the rear rotor arm angle is θ = 20°, strong thrust fluctuation is observed from ψ = 300° to ψ = 40° in both Figure 11 and Figure 12. This indicates that the wake interaction causes unsteady loading on the front rotor.

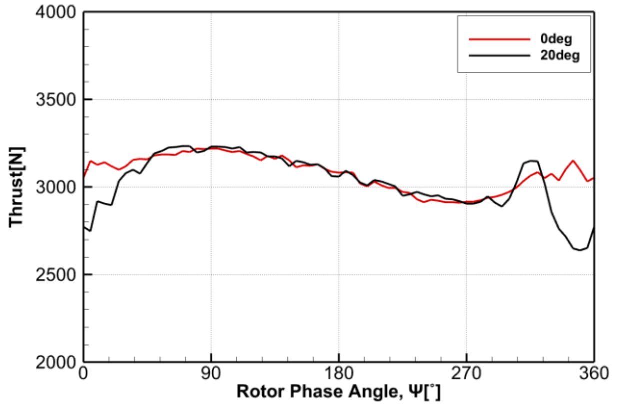

Figure 12: Thrust of blade with different location of rear rotor

Figure 13 presents the 1/2 peak-to-peak thrust fluctuation according to the position of the rear rotor. Figure 13 distinguishes between the front rotor, rear rotor, and the full configuration. As the height of the rear rotor increases, the peak-to-peak of thrust fluctuation for the front rotor and full configuration tends to increase, while it is confirmed to decrease for the rear rotor. Compared to θ = 0°, the 1/2 peak-to-peak value for the front rotor increased by more than two times for θ = 20°, while it decreased by 63% for the rear rotor. This explains that the thrust fluctuation of the front rotor was distinct significantly due to the strong interaction of rotor wake. In contrast, the thrust fluctuation of the rear rotor, which is less influenced by the wake interaction, decreased somewhat. Overall, the 1/2 peak-to-peak value for the full configuration increases by 37%, indicating that the increase in the front rotor's thrust fluctuation is more dominant than the decrease in the rear rotor's thrust fluctuation.

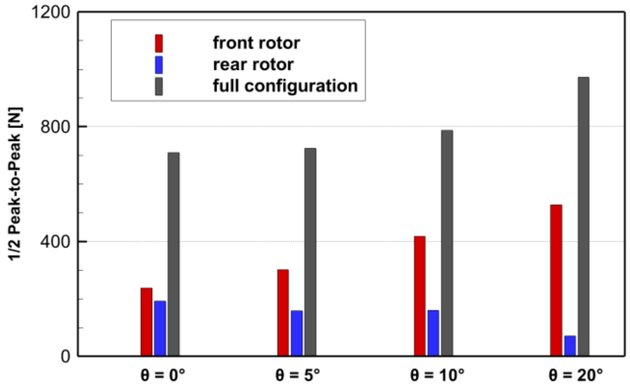

Figure 13: 1/2 peak-to-peak of thrust fluctuation with different location of rear rotor

The mutual interaction from rotor wake varied depending on the position of the rear rotor. This wake interaction influences the noise source of the quadrotor. Figure 14 displays the instantaneous dilatation field in the rotor region based on the position of the rear rotor. When the rear rotor arm angle is 0°, symmetric noise radiation is observed in both regions of the front and rear rotor. However, as the height of the rear rotor increases, an asymmetric phenomenon is observed in the front rotor region. In particular, Figure 14(d) shows intense tonal noise and widely radiated noise sources in the front rotor region. It is estimated that the strong wake interaction in the front rotor region, observed in Figure 8(d), induces unsteady loading on the front rotor, which likely leads to unsteady loading noise. Therefore, as shown in Figure 14(d), it is concluded that the sound intensity from the front rotor increases and the noise radiation becomes widespread.

To quantitatively compare the noise level based on the position of the rear rotor, the overall sound pressure level (OASPL) is compared. First, the OASPL at the M6 microphone position is shown in Figure 15, distributed by the front rotor, fuselage, rear rotor, and full configuration. It is observed that as the height of the rear rotor increases, the noise level of the front rotor and the full configuration tends to increase. The noise generated from the fuselage and the rear rotor decreases somewhat, likely because the wake interaction occurs in the fuselage region when θ = 0°, as shown in Figure 8(a).

Figure 16 provides the OASPL of the front rotor and the full configuration at all microphone positions with azimuth angle. As shown in Figure 16(a), it can be observed that the noise level increases at all microphone positions as the rear rotor is positioned higher.

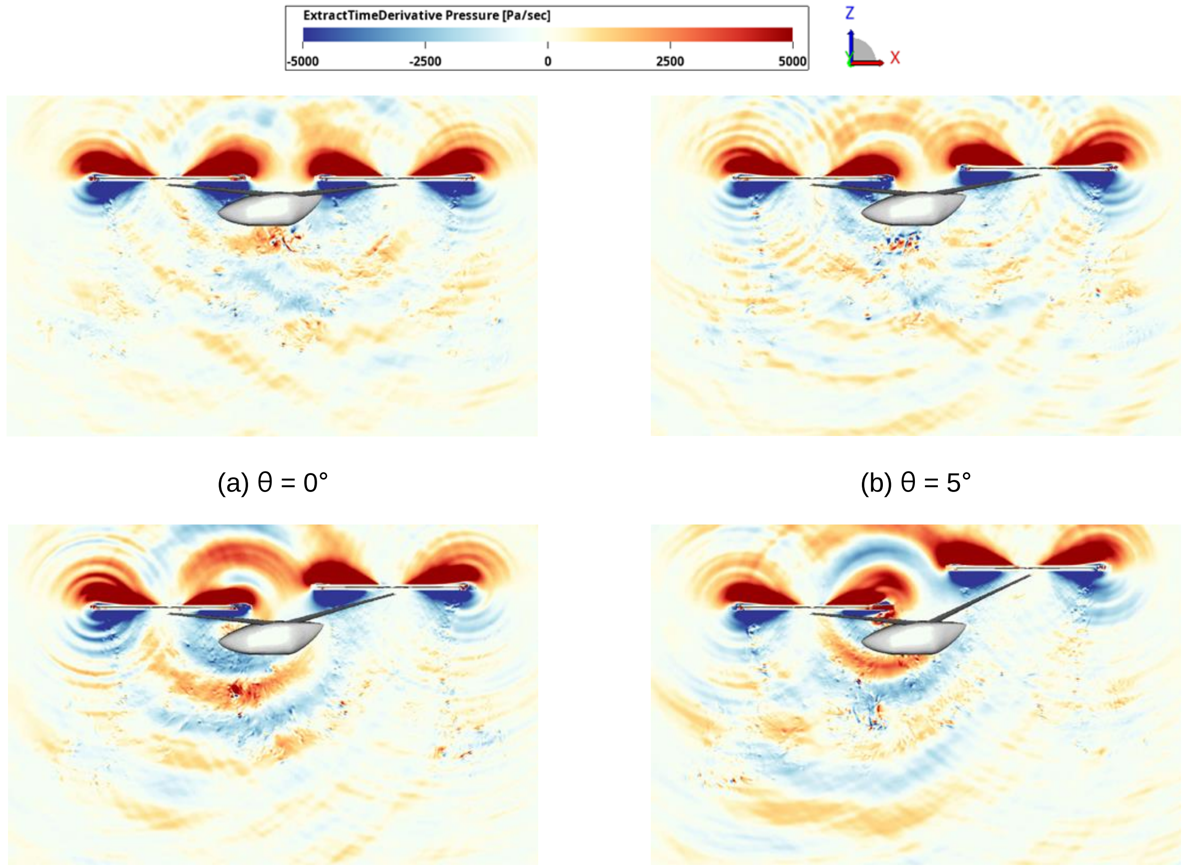

(a) θ = 0°

(b) θ = 5°

(c) θ = 10°

(d) θ = 20°

Figure 14: Comparison of instantaneous dilatation field with different location of rear rotor

When the rear rotor arm angle is 20°, the noise level increases on average by approximately 2 dB compared to when the rear rotor arm angle is 0°. The increase in noise level is likely due to the gradually stronger unsteady loading noise caused by the wake interaction. The increased noise level from the front rotor leads to an increase in the noise level of the full configuration, as shown in Figure 16(b). It is observed that the noise level increased by an average of 1 dB from θ = 0° to θ = 20°.

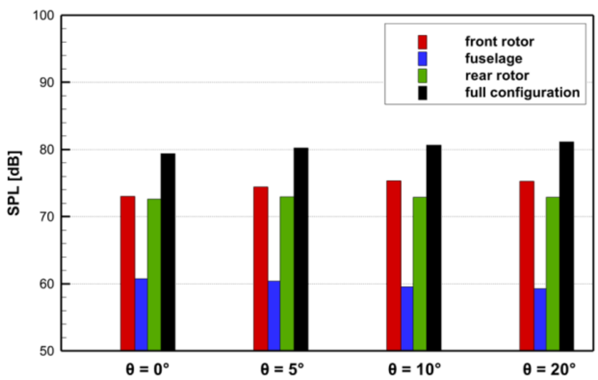

Figure 15: Comparison of OASPL with different location of rear rotor at M6 microphone

Figure 17 demonstrates the noise level and directivity based on the position of the rear rotor using the noise hemisphere. The noise hemispheres are presented in two views: a top view, looking down on the configuration, and an iso view, showing the three-dimensional perspective. In all cases with the different rear rotor arm angles, the noise directivity radiates widely to the region below the quadrotor due to loading noise in common. As the height of the rear rotor increases, it is observed that the noise level from the region below the aircraft increases and tends to radiate more widely.

6. Conclusions

This study employed aerodynamic and acoustic analyses on quadrotor AAV configuration with varying the rear rotor arm angles. The computational investigations were performed using the high-fidelity LBM simulation. The acoustic predictions were carried out using the FW-H acoustic analogy with an impermeable surface. Through aerodynamic analysis of the rotor, disparity of the noise depending on the position of the rear rotor was confirmed, and the noise level of each component was compared. The conclusions drawn based on the results obtained from this study are as follows:

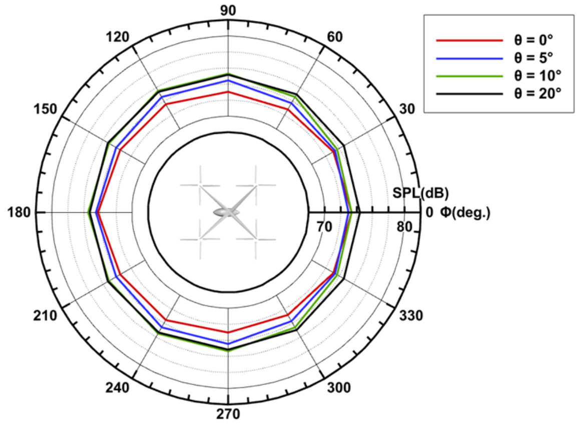

(a) Front rotor

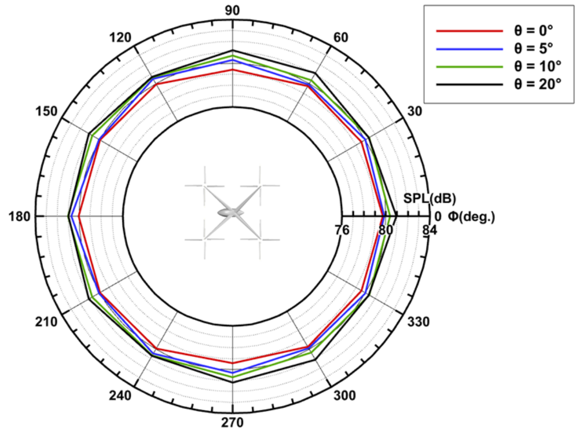

(b) Full configuration

Figure 16: OASPL with different location of rear rotor

1. The wake interaction effects varied depending on the position of the rear rotor, and stronger mutual interference was observed in the front rotor region as the height of the rear rotor increased. This is likely because the wake of the rear rotor was ingested by the front rotor.

2. At θ = 20°, the wake interaction imposed the effects of upwash on the front rotor. This upwash flow induced unsteady loading on the front rotor, which resulted in strong thrust fluctuation on the front rotor. Although the thrust fluctuation of the rear rotor decreased somewhat, the strong thrust fluctuation of the front rotor resulted in distinct thrust fluctuation of the full configuration.

3. The unsteady loading originating from the wake interaction resulted in an unsteady loading noise of the front rotor. As the rear rotor was positioned higher, asymmetric noise radiation was observed, and the noise level from the front rotor increased by approximately 2 dB.

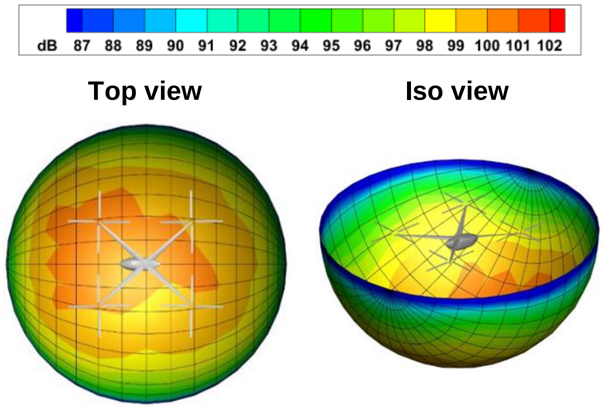

(a) θ = 0°

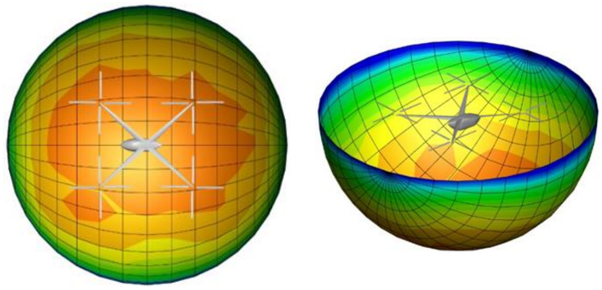

(b) θ = 5°

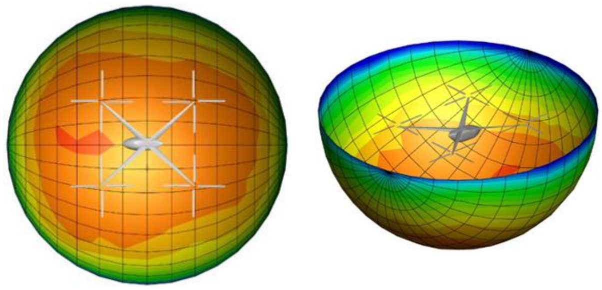

(c) θ = 10°

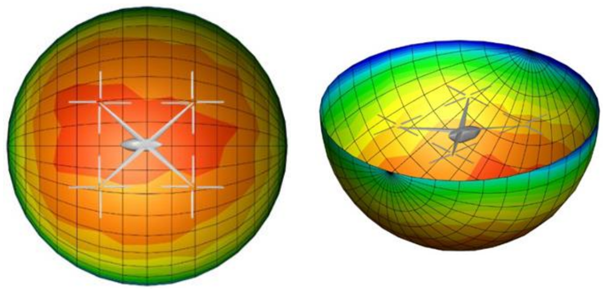

(d) θ = 20°

Figure 17: Comparison of noise hemisphere with different location of rear rotor

Since this study was conducted in hovering conditions, it is necessary to investigate the rotor interaction during forward flight. When considering forward flight conditions, the aerodynamic and noise changes of the AAV will be examined based on its mission profile. Finally, this paper only considered tonal noise, so the changes in broadband noise from wake interaction will be investigated in future work.

Author contact:

Yu Hyeon Hwang simonzz98@gnu.ac.kr

Si Jin Kim eunmin9707@gnu.ac.kr

Hyeon Su Song skzkek33@gnu.ac.kr

Rho Shin Myong myong@gnu.ac.kr

Hakjin Lee hlee@gnu.ac.kr

7. ACKNOWLEDGMENTS

This research was supported by Regional Innovation Mega Project program through Korea Innovation Foundation funded by Ministry of Science and ICT (2023-DD-UP-0026). This work was supported by the National Research Foundation of Korea (NRF) grant funded by the Korea government (MSIT) (RS-2024-00397400)

8. REFERENCES

1. Silva, C., Johnson, W. R., Solis, E., Patterson, M. D., and Antcliff, K. R., “VTOL Urban Air Mobility Concept Vehicles for Technology Development,” *In 2018 Aviation Technology*, Integration, and Operations Conference, 2018, p. 3847.
2. Higgins, R. J., Barakos, G.N., Shahpar, S., and Tristanto, I., “A Computational Fluid Dynamic Acoustic Investigation of a Tiltwing eVTOL Concept Aircraft,” *Aerospace Science and Technology*, Vol. 111, 2021, 106571.
3. Zahn, D., Naru, R., Guion, A., and Eggum, S., “UAM Instrument Flight Procedure Design and Evaluation in the Joby Flight Simulator,” No. AAM-NC-115-001, 2023.
4. Duffy, M. J., Wakayama, S. R., and Hupp, R., “A Study in Reducing the Cost of Vertical Flight with Electric Propulsion,” *In 17th AIAA Aviation Technology, Integration, and Operations Conference*, 2017, p.3442.
5. Zhou, W., Ning, Z., Li, H., and Hu, H., “An Experimental Investigation on Rotor-to-Rotor Interactions of Small UAV Propellers,” *In 35th AIAA applied aerodynamics conference*, 2017, p.3744.
6. Piccinini, R., Tugnoli, M., and Zanotti, A., “Numerical Investigation of the Rotor-Rotor Aerodynamic Interaction for eVTOL Aircraft Configurations,” *Energies*, Vol. 13(22), 2020, 5995
7. Herz, S., Atte, A., Seth, D., Rauleder, J., and McCrink, M., “Impact of Rotor-Rotor and Rotor-Body Aerodynamic Interactions on Quadrotor Vehicle Performance,” *In VFS 79th Annual Forum*, 2023.
8. Alvarez, E. J., and Ning, A., “High-Fidelity Modeling of Multirotor Aerodynamic Interactions for Aircraft Design,” *AIAA Journal*, Vol. 58(10), 2020, 4385-4400.
9. Stokkermans, T. C., Usai, D., Sinnige, T., and Veldhuis, L. L., “Aerodynamic Interaction Effects between Propellers in Typical eVTOL Vehicle Configurations,” *Journal of Aircraft*, Vol. 58(4), 2021, 815-833.
10. Hill, B. P., DeCarme, D., Metcalfe, M., Griffin, C., Wiggins, S., Metts, C., … and Mendonca, N. L., “Uam Vision Concept of Operations (conops) Uam Maturity Level (uml) 4, 2020
11. Greenwood, E., Brentner, K. S., Rau, R. F., and Ted Gan, Z. F., “Challenges and Opportunities for Low Noise Electric Aircraft,” *International Journal of Aeroacoustics*, Vol. 21(5-7), 2022, 315-381.
12. Ahuja, V., Little, D. S., Majdalani, J., and Hartfield, R. J., “On the Prediction of Noise Generated by Urban Air Mobility (UAM) vehicles. II. Implementation of the Farassat F1A Formulation into a Modern Surface-Vorticity Panel Solver,” *Physics of Fluids*, Vol. 34, 2022.
13. Casalino, D., van der Velden, W. C., and Romani, G., “Community Noise of Urban Air Transportation Vehicles,” *In AIAA Scitech 2019 Forum*, 2019, p. 1834.
14. Casalino, D., van der Velden, W. C., Romani, G., and Gonzalez-Martino, I., “Aeroacoustic Analysis of Urban Air Operations Using the LB/VLES Method,” *In 25th AIAA/CEAS Aeroacoustics Conference*, 2019, p. 2662.

15. Yunus, F., Casalino, D., Avallone, F., and Ragni, D., "Efficient Prediction of Urban Air Mobility Noise in a Vertiport Environment," *Aerospace Science and Technology*, Vol. 139, 2023, 108410.

16. Jia, Z. H., and Lee, S., "Computational Study on Noise of Urban Air Mobility Quadrotor Aircraft," *Journal of the American Helicopter Society*, Vol. 67(1), 2022, 1-15.

17. Lee, H., and Lee, D. J., "Rotor Interactional Effects on Aerodynamic and Noise Characteristics of a Small Multirotor Unmanned Aerial Vehicle," *Physics of Fluids*, Vol. 32(4), 2020.

18. Jia, Z. H., and Lee, S., "High-Fidelity Computational Analysis on the Noise of a Side-by-Side Hybrid VTOL Aircraft," *Journal of the American Helicopter Society*, Vol. 67(2), 2022, 1-14.

19. Zhang, T., Barakos, G. N., and Foster, M., "High-Fidelity Aerodynamic and Acoustic Design and Analysis of a Heavy-Lift eVTOL," *Aerospace Science and Technology*, Vol. 137, 2023, 108307.

20. Afari, S. O., and Mankbadi, R. R., "Simulations of multi-rotor interaction noise at hovering & forward flight conditions," *International Journal of Aeroacoustics*, Vol. 22(1-2), 2023, 153-187.

21. Teruna, C., Avallone, F., Casalino, D., and Ragni, D., "Numerical Investigation of Leading Edge Noise Reduction on a Rod-Airfoil Configuration Using Porous Materials and Serrations," *Journal of Sound and Vibration*, Vol. 494, 2020, 115880.

22. Teruna, C., Avallone, F., Ragni, D., Rubio-Carpio, A., and Casalino, D., "Numerical Analysis of a 3-D Printed Porous Trailing Edge for Broadband Noise Reduction," *Journal of Fluid Mechanics*, Vol. 926, 2021, A17.

23. Kotapati, R. B., Shock, R., and Chen, H., "Lattice-Boltzmann Simulations of Flows over Backward-Facing Inclined Steps," International Journal of Modern Physics C, Vol. 25(01), 2014, 1340021.

24. Chen, S., and Doolen, G. D., "Lattice Boltzmann Method for Fluid Flows," *Annual review of fluid mechanics*, Vol. 30(1), 1998, 329-364.

25. Bhatnagar, P. L., Gross, E. P., and Krook, M., "A Model for Collision Processes in Gases. I. Small Amplitude Processes in Charged and Neutral One-Component Systems," *Physical review*, Vol. 94(3), 1954, 511.

26. Hecht, M., and Harting, J., "Implementation of On-Site Velocity Boundary Conditions for D3Q19 Lattice Boltzmann Simulations," *Journal of Statistical Mechanics: Theory and Experiment*, Vol. 2010(01), 2010, P01018.

27. Yakhot, V., and Orszag, S. A., "Renormalization Group Analysis of Turbulence. I. Basic Theory," *Journal of scientific computing*, Vol. 1(1), 1986, 3-51.

28. Chen, H., Kandasamy, S., Orszag, S., Shock, R., Succi, S., and Yakhot, V., "Extended Boltzmann Kinetic Equation for Turbulent Flows," *Science*, Vol. 301(5633), 2003, 633-636.

29. Teruna, C., Rego, L., Casalino, D., Ragni, D., and Avallone, F., "A Numerical Study on Aircraft Noise Mitigation Using Porous Stator Concepts," *Aerospace*, Vol. 9(2), 2022, 70.

30. Kim, S. J., Hwang, Y. H., Myong, R. S., and Lee, H., "Interactional Aerodynamics and Acoustics of a Rotor with an Airframe in Hover," *Physics of Fluids*, Vol. 36(1), 2024.

31. Williams, J. F., and Hawkings, D. L., "Sound Generation by Turbulence and Surfaces in Arbitrary Motion," *Philosophical Transactions for the Royal Society of London. Series A, Mathematical and Physical Sciences*, 1969, 321-342.

32. Li, X. D., and Zhou, S., "Spatial Transformation of the Discrete Sound Field from a Propeller," *AIAA journal*, Vol. 34(6), 1996, 1097-1102.

33. Brentner, K. S., and Farassat, F., "Modeling Aerodynamically Generated Sound of Helicopter Rotors," *Progress in aerospace sciences*, Vol. 39(2-3), 2003, 83-120.

34. Silva, C., Johnson, W. R., Solis, E., Patterson, M. D., and Antcliff, K. R., "VTOL Urban Air Mobility Concept Vehicles for Technology Development," in *2018 Aviation Technology, Integration, and Operations Conference*, 2018, p.3847.

35. Thurman, C. S., Zawodny, N. S., and Baeder, J. D., "Computational Prediction of Broadband Noise from a Representative Small Unmanned Aerial System Rotor," *in 76th Annual Forum & Technology Display*, 2020.